Spectral unmixing model to assess land cover fractions in Mongolian steppe regions.

Ishgaldan Byambakhuu [a], Michiaki Sugita [a] and Dai Matsushima [b]

[a]Doctoral Program in Geoenvironmental Sciences, Graduate School of Life and Environmental Sciences, University of Tsukuba, Ibaraki 305-8572, Japan

[b]Department of Architecture and Civil Engineering, Chiba Institute of Technology, Chiba 275-0016, Japan

email: ibyamba@geoenv.tsukuba.ac.jp and sugita@geoenv.tsukuba.ac.jp

Abstract

The land cover fractions (LCFs) and spectral reflectance of photosynthetic vegetation (PV), nonphotosynthetic vegetation (NPV), and bare soil were measured at 58 sites in semi-arid and arid regions of Mongolia in the summers of 2005 and 2006. These data sets allowed a detailed assessment of the impact of measurement geometry as represented by the solar zenith angle θ_s, sensor view zenith angle θ_v, and azimuth view angle ϕ in the estimation of LCF values by means of the spectral unmixing model (SUM). The bidirectional distribution function (BRDF) was fitted to the reflectance data and then used to produce reflectance at various measurement geometry. LCFs from these reflectance data for a given combination of θ_s, θ_v, and ϕ were compared with visually determined LCFs. It was found that θ_s in the range of 30-45° produced a better agreement of LCFs. For θ_v, the agreement is not very sensitive to the choice of angle for the range 30-70°, although θ_v = 50° showed a slightly better performance. The azimuth view angle does not have strong influences to the LCF estimation, except for the case of ϕ = 180° (view toward the sun), which does not allow precise fitting of BRDF function over a tall vegetation site. Overall, this study verified the results of earlier studies obtained mostly for the American continents that SUM is capable of producing LCF estimates accurately and also found that its accuracy was, in general, much better than that by the more traditional approach of the supervised classification method (SCM) applied to images of a digital camera.

Keywords: Mongolia; semiarid and arid area; BRDF; viewing geometry; land cover fractions; spectral unmixing model

1. Introduction

In terrestrial ecosystem, land cover plays an important role in the transfer of energy, momentum, and scalar admixture such as water vapor between the Earth's surfaces and the atmosphere. This, in turn, affects the magnitude and timing of carbon fixation, respiration, and nutrient cycles. It is thus essential to evaluate the land cover fractions (LCFs) of photosynthetic vegetation (PV), nonphotosynthetic vegetation (NPV), and bare soils. However, it has been found difficult to estimate LCFs with traditional approaches. For example, photograph images have been used to classify the surface covers by means of the supervised classification method (SCM) (White et al., 2000; Li et al., 2005), the ocular estimation, the sampling belt, and the photographic methods (Li et al., 2005). However, Zhou et al. (1998) have shown that different methods may lead to significantly different outcomes particularly when the target area is large. Similarly, multi-channel sensors aboard satellite have also been used for this purpose because it is desirable to utilize remote sensing technology for the assessment and monitoring of LCFs over larger areas and over a long period. Again, usefulness of these traditional sensors for this purpose has been found to be limited in many cases (Asner & Lobell, 2000; Carlson & Ripley, 1997). The main difficulty stems from the coarse horizontal resolution of these sensors. A typical scale of horizontal variations of LCFs is often much smaller than the pixel size of the satellite sensors.

As an alternative approach, the spectral unmixing model (SUM) has been developed to derive LCFs of PV, NPV, and bare soil covers at the sub-pixel level from a pixel mean reflectance $\overline{\rho_p}(\lambda)$ measured at wavelength λ. The determination of sub-pixel LCFs relies on an endmember analysis (Asner & Lobell, 2000). In the present case, the endmembers are the spectral reflectance $\rho_i(\lambda)$ (for i = 1 to 3) of PV, NPV, and bare soil, and $\overline{\rho_p}(\lambda)$ is assumed to be given as a weighted average of $\rho_i(\lambda)$ by

$$\overline{\rho_p}(\lambda) = \sum_{i=1}^{n} \left[C_i \cdot \rho_i(\lambda) \right] + \varepsilon \qquad (1)$$

where the weighting factors C_i is the cover fraction of the i-th land cover component to be determined, and $\sum_{i=1}^{n} C_i = 1$. ε is the error term. Because the number of endmember is three, in theory, the reflectance data at the minimum of two wavelengths should allow determination of LCFs. With multi-channel or hyperspectral measurements, this can be accomplished. Usually, there are a redundant, large number of possible selections of λ, particularly for hyperspectral measurements, and a wide range of acceptable unmixing could be obtained. This has been solved by employing Monte Carlo analysis to account for the natural variability of endmembers through the calculation of uncertainty for each pixel endmember constituents (Asner & Lobell, 2000; Asner & Heidebrecht, 2002). Thus, the mean and the standard deviation of the derived values for each LCF are determined from large number of λ combinations, and not only the estimates of LCFs but also some indication of accuracy can be obtained. Other proposals to make use of this large number of combinations have also been made (e.g., Chen et al., 2009).

As outlined above, the general framework of this approach is straightforward, and there is a potential to apply this method to determine LCFs from images taken remotely by the aircraft or satellite. In fact, Asner and Lobel (2000) and Lobell et al. (2002) have successfully tested the applicability of this method with the data set obtained by the airborne instrument above the test sites in US. However, there are several issues that need to be addressed before such an application over even larger areas becomes acceptable. Among them, one concern is a possibility that spectral endmembers that have been found to produce LCF estimates well for one region may not be applicable to other regions. Therefore, careful examinations of this method in a wide range of areas and surface conditions are essential. The SUM approach has been tested mostly in the American ecosystems, and not much is known on the applicability to the other regions of the world.

Second, spectral data are usually obtained at a certain combination of sensor view geometry and solar position, and not much is known on the influence of the selection of these angles to the final LCF estimates. For example, the only study that treated the effects of sensor view angles is probably that by Lobell et al. (2002). They found that the variability in LCFs due to the change of sensor view angle was small when the SUM was applied with hyperspectral images. To our knowledge, the influence of the different solar position on the land cover estimates has not been studied. A common approach to avoid this second issue is to carry out observations at the time of the same or similar solar position. For example, the field observations could be restricted for only around noon of each day in the same season of the year. However, such observation is quite time consuming as only certain portion of the day or season can be spent for actual measurements. Moreover, for satellite or aircraft measurements, this is impractical because the choice of the observation (i.e., overpass) time is limited or nonexistent on the observer's side. For observations to be carried out at any time of the daylight hours, it is necessary to investigate the impact of the solar position to the final estimates. If the effects are found not negligible, it is further necessary to correct or minimize such effect on to the final LCF determination.

These are the brief background of LCF estimates by means of the SUM approach. To shed some light on these remaining problems in this approach, particularly on the effects of measurement geometry to the LCF estimates, an attempt was made to use bidirectional distribution function (BRDF) to convert reflectance taken at arbitrary view angles to a predetermined standard condition. This way, the effects of the measurement geometry can be studied in a consistent manner and for the sensor view geometry and solar angles not encountered during actual measurements. For the data acquisition, field experiments were carried out in one of the least studied regions of the world, Asian steppe region in Mongolia. The steppe extends further towards central Asia, and as a whole, it constitutes the largest grasslands belt region on earth (Shiirevdamba, 1998). Therefore, a test in this region should benefit to increase the extent of areas where the usefulness of the SUM approach has already been established. As a reference of the test of the LCF estimates by means of SUM approach, those estimates from digital camera image based on more conventional supervised classification method (SCM) were also derived. This is one of the methods that is most commonly accepted at present (White et al., 2000).

2. Methods

2.1 Experimental areas and sites

The experiment was carried out in the summers of 2005 and 2006 in Mongolia, which is covered mostly (by some 90%; Shiirevdamba, 1998) with steppe vegetation where nomadic animal husbandry is the main land use. Seven study areas were selected in semi-arid and arid regions of Mongolia (Fig. 1) to cover a wide variety of vegetation groups. Most of the areas in the semi-arid region are located within and around the Kherlen river basin (48° 30' N - 46° 30' N and 108° 15' E - 110° 45' E) in the northeastern part of Mongolia. The annual precipitation ranges from 150 to 300 mm (Saandar & Sugita, 2004), and more than 70% of precipitation fall only during the summer period from June to August. The vegetation in this region is a typical short-grass steppe and is dominated mostly by the cool season C_3 (mainly *Stipa krylovii, Carex duriuscula, Artemisia adamsii, Artemisia frigid, Leymus chinensis, and*

Caragana microphylla) and some C_4 species (*Cheistogenes squarrosa*) (Li et al., 2005). The details of this region are described in Sugita et al. (2007) and in related studies in the same special issue for the Rangeland Atmosphere–Hydrosphere-Biosphere Interaction Study Experiment in Northeastern Asia (RAISE) project (Sugita et al., 2007), from which the data sets used for this study were obtained. In the southern arid region, two study areas of Bulgan in Southern Gobi (44° 25' N - 44° 01' N and 103° 57' E - 103° 70' E) and of Mandalgobi (45° 94' N - 45° 67' N and 106° 23' E - 106° 47' E) were selected as the targets for the field measurements. The annual precipitation here ranges from 100 to 150 mm (Sasaki et al., 2005).

Within each study area, the sites for the actual measurements were selected at random, but it was ensured that each site represents, and is at the center of, the homogeneous (in a statistical sense, meaning that the surface variability is sufficiently small and constant in space; Brutsaert, 1998) vegetation of greater than 1 m^2 and that overall selections produce a wider variety of different combinations of LCFs and vegetation species. As a result, a total of 58 sites (34 from the semi-arid study area and 24 from the arid study areas) were selected for this study. They are listed in Table 1 together with the other relevant information such as vegetation height, species, and biomass.

2.2. Field observations

2.2.1. Land cover survey

At the center of each site, a 0.5 × 0.5–m quadrat was constructed, and a land cover survey of the quadrat was carried out. First, the LCFs in terms of the percentages of PV, NPV, and bare soil were visually determined from 1 m above the surface. In the present analysis, they were served as true LCFs to be compared with those from SUM and also from SCM. To obtain as consistent and unbiased estimates of LCFs as possible, the same person always carried out the visual determination at all sites. Second, photographs were taken by means of a digital camera (Canon IXY400, 4 mega pixels) at a nadir-looking position from 1 m above the surface. The instantaneous field of view (IFOV) of the digital camera was 0.42 m^2. Finally, after the spectral radiance measurement (see below), all PV and NPV parts were removed by a clipping method, and the digital camera image and spectral radiance data of the soil surface were similarly obtained. As background information, the mean surface soil moisture (0-12 cm) was determined by means of a time-domain reflectometry (TDR) sensor (Campbell Scientific, HydroSense), and the vegetation samples were later oven dried, and their weight (dry biomass) was measured. The surface soil moisture could be important because it affects the color of vegetation and soil; biomass is an alternative indicator of the land cover.

2.2.2. Spectral reflectance

The spectral reflectance of the site was measured within the wavelength of 350 to 2500 nm with resolution of 10 nm, by a spectroradiometer (FieldSpec Pro, Analytical Spectral Devices, Inc.) with an 8°-sensor foreoptic attached. The radiometer height was fixed at 1.5 m above the surface, except for the case of θ_v = 0 for which it was at 1.0 m. The IFOV was 0.03 m^2 for sensor view zenith angle θ_v = 0° (nadir position), 0.08 m^2 for θ_v = 30°, 0.24 m^2 for θ_v = 50°, and 0.93 m^2 for θ_v = 70°. This way, IFOV of the radiometer always includes the selected 0.5 × 0.5–m quadrat, and the view within IFOV consists of the same land cover represented by the quadrat, for all selected sensor off-nadir viewing angles.

The experiment at each site included the bidirectional spectral reflectance measurements at eight azimuth view angles starting from the solar direction (ϕ = 0°) and every 45° from ϕ = 0°, and at θ_v of 30°, 50°, and 70° at each azimuth angle. This, together with the measurements at a nadir-looking position θ_v = 0, produced 25 bidirectional reflectance data sets within approximately 20 minutes at each site. The mean directional radiance was divided by the incoming components measured as reflected radiance by a white reference panel, to derive the surface reflectance. Note that some papers refer this as the hemispherical-directional reflectance (e.g., Painter and Dozier, 2004).

Once the reflectance measurements had been completed, the vegetation within the 0.5 × 0.5–m quadrat was removed by a clipping method. In this operation, PV and NPV were removed carefully so as to minimize the disturbance to the underlying soil surface.

Then, the spectral reflectance of the soil surface was measured from a nadir-looking position. In addition, the spectral reflectance of the vegetation itself was measured by the same spectroradiometer with the samples removed from the quadrat but with a contact probe option (Analytical Spectral Devices, Inc.) attached. The observations were performed from approximately 8:00 to 18:00 local solar time (LST). A total of 58 effective series of data were obtained in the intensive observation.

2.3. Bidirectional reflectance function

A BRDF gives reflectance ρ as a function of θ_v, ϕ, and the solar zenith angle θ_s, and thus with BRDF determined, it is possible to convert radiance of any arbitrary measurement geometry of θ_s, θ_v, and ϕ at the time of measurement, into those of the other arbitrarily selected geometries. There have been many efforts to develop a BDRF model (e.g., Kimes, 1983; Roujean et al., 1992; Rahman et al., 1993a,b; Susaki et al., 2004). In this study, Rahman's model was adopted as this model can be applied to spectral reflectance data collected both from the field and through remote sensing (Privette et al., 1997; Matsushima et al., 2005). The BRDF equations are formulated as follows:

$$\rho(\theta_s, \theta_v, \phi) = \rho_0 \frac{\cos\theta_s^{\kappa-1} \cos\theta_v^{\kappa-1}}{(\cos\theta_s + \cos\theta_v)^{1-\kappa}} F(g)[1+R] \qquad (2)$$

$$F(g) = \frac{1-\Theta^2}{\left[1+\Theta^2 - 2\Theta\cos(\pi - g)\right]^{1.5}} \quad (3)$$

$$R = \frac{1-\rho_0}{1+\left[\tan^2\theta_s + \tan^2\theta_v - 2\tan\theta_s \tan\theta_v \cos\phi\right]^{\frac{1}{2}}} \quad (4)$$

$$g = \cos\theta_s \cos\theta_v + \sin\theta_s \sin\theta_v \cos\phi \quad (5)$$

where R represents the hot spot effect, which is used to describe the peak in reflectance that occurs in the retro-reflection direction when the sun is located directly behind the sensor and shadowing is zero. Three unknown parameters of Θ, ρ_0 and k can be determined through a least squares regression with a set of observed reflectance data.

2.4. Spectral unmixing model

The main equation for the spectral unmixing model can be written by (1). As mentioned, given the values of $\overline{\rho_p}(\lambda)$ and three endmembers $\rho_i(\lambda)$ for at least two different wavelengths, the LCF value C_i for PV, NPV, and bare soil should be able to be determined from (1). In practice, there are 200 possible selections of λ for the present data set. Thus, the Monte Carlo technique was employed to generate a large number of combinations by randomly selecting spectra from the 200 reflectance data sets, by following Asner & Lobell (2000). They performed a sensitivity analysis and identified the minimum optimum number of combinations of spectra as 50. The same analysis was carried out with our data set. The results verified their finding. Thus, the LCF values were determined for 50 selections, and their mean and the standard deviation were recorded in the analysis.

2.5. Supervised classification method applied to digital camera images

As mentioned, LCF estimates with digital camera images by means of SCM, an example of more traditional approaches, will be used as a reference, against which the performance of SUM will be compared. SCM is a general classification scheme based on pre-defined classes and training areas. Thus a user sets up classes within an image and assigns a training area of each class based on prior knowledge. In this study, SCM was implemented by the algorithm with the maximum likelihood technique built within the image processing software (ERDAS IMAGINE 9.1, Leica Geosystems). In the application, first, the 0.5 × 0.5–m quadrat part of the image was extracted from the original larger image. Then, the IHS (intensity, hue, and saturation) transformation was applied for all extracted images before the SCM application. This was based on the results of a preliminary analysis to test SCM performance with both RGB (red, green, and blue) and IHS images. It was found that IHS images produced much better results (not shown here). Third, to distinguish the LCFs, a training area of each class was created in the extracted image, and then, three signatures (i.e., homogeneous sample pixels) were generated from the training areas of each

LCF class. Finally, after having obtained satisfactory discrimination between the LCF classes, LCFs were derived for each image.

3. Results and discussion

3.1. Performance of BRDF

As mentioned earlier, for the application of BRDF conversion, Eqs. (2)-(5) were fitted to a set of raw reflectance data for each site to determine the site-specific three parameters of Θ, ρ_0, and *k*. Once these parameters are obtained, the conversion is straightforward, and reflectance at any arbitrarily selected combination of angles of measurement geometry, ϕ, θ_s, and θ_v can be produced. To test the performance, the BRDF was determined for each of the 58 sites; then, the converted spectral reflectance data were reproduced for the 12 combinations of ϕ (0, 90, 180, and 270°) and θ_v (30, 50, and 70°) for each site. These were compared with those measured raw reflectance at the selected same angles of ϕ and θ_v. The total of 693 data points produced a good agreement (Fig. 2), with r = 0.89, root mean square error (RMSE) of 0.037, systematic RMSE of 0.019, and unsystematic RMSE of 0.018 (Willmott, 1982). Thus, in general, the BRDF in the form of (2)-(5) is capable of reflectance conversion for a range of measurement geometry. Note that the measured surface reflectance in this study is not exactly the bidirectional reflectance, since the incoming radiation measured through white reflectance panel is the hemispherical radiation composed of diffuse and direct components. The success of BRDF application probably indicates that the majority of the radiation is the direct component, and the diffuse part is of lesser importance. Three outlier points can also be noted in Fig.2. They are all for one particular site (KBU11) and for one particular view angle of ϕ = 180°. A closer look at the vegetation information (Table 1) and the reflectance data has shown that it was probably caused by much denser and taller vegetation of this site. When vegetation height increases, the amount of shadow tends to increase within the sensor view, and it looks differently depending on how sensor is aimed at the target. Moreover, when ϕ = 180° and the sensor aims directly in the direction of the sun, it is most susceptible to the effect of forward scattering (Kimes, 1983). This effect is more pronounced for taller and denser vegetation cover. Thus, it is probably safe to avoid ϕ at approximately 180° particularly for a site with tall vegetation.

3.2 Derivation of LCFs from SUM with BRDF

Sample and reflectance type selections

To apply SUM, first, it is necessary to decide what parts of wavelength and what type of spectra should be used. Asner & Lobell (2000) noted that spectral reflectance of PV, NPV, and soil varied little within the wavelength of 2100-2400 nm in the SWIR (short-wave infrared) region and used the reflectance within this wavelength region to apply the SUM approach. A preliminary examination of the spectral data sets obtained in this study confirmed their assessment. Therefore, the same spectral region of 2000-2400 nm was used. Asner & Lobell (2000) also examined possibilities to use three types of spectral data, namely, the raw reflectance $\rho(\lambda)$, the derivative reflectance $d\rho(\lambda)/d\lambda$, and the tied reflectance $\rho(\lambda)-\rho_0$ in which ρ_0 is called the tied point. Examples of these tree types of reflectance for PV, NPV, and bare soil within the SWIR region are plotted in Fig. 3. Among these three, Asner and Lobell (2000) recommend the use of the tied spectra based on the sensitivity test to the noise. Their noise propagation analysis was also repeated here with the current data sets, with ρ_0 = 2075 nm selected. The same results (not shown) were derived—the tied reflectance is the least sensitive to the noise. Therefore, it was also decided to use the tied spectra in the following analysis, and thus, $\overline{\rho_p}(\lambda)$ and endmembers $\rho_i(\lambda)$ in (1) should now represent the mean tied spectra within the sensor's view and the tied reflectance of the *i*-th land cover component, respectively, both at wavelength λ.

For the implementation of SUM, specific samples whose reflectance $\rho_i(\lambda)$ (i = 1 to 3) are to be used as endmembers for PV, NPV, and bare soil need to be determined. For the NPV, the reflectance of a single NPV sample, which was arbitrarily selected from all NPV samples, was adopted based on the observation that the shape and magnitude of spectra of all NPV samples were very similar. For the bare soil, the reflectance determined at each site was used as the endmember. The PV endmember reflectance was taken from the sample of the most common species within each experimental area, namely *Stipa krylovii* for the semi-arid area and *Allium mongolicum* for the arid region. A test with a different vegetation selection, that is, with *Carex duriuscula* and *Allium polyrhizum* as the sample for the PV endmember reflectance did not change the final results significantly. Thus, the choice of vegetation species that represent the spectra of PV and NPV is probably irrelevant in the estimates of LCFs. This is probably because all observations were carried out in a relatively short period in summer, and the spectral characteristics of vegetation remain quite similar, regardless of species. If observations had spanned over different seasons or plant life-cycle stages, the results could have been more sensitive to the choice of PV and NPV endmembers.

Impact of measurement geometry

With the tied spectra in the SWIR region, first, the effects of the solar zenith angles on the determination of LCFs by means of SUM were examined. For this analysis, first, a data set of the bidirectional reflectance observed over the same vegetation species but at multiple locations and at different solar zenith angles were selected. This data set allowed BRDFs (2)-(5) to be specified for the particular vegetation. Among the observations, those measured over the four species of *Stipa krylovii* (at 9 sites), *Leymus chinesis* (5 sites), *Cleoistogenes squarrosa* (5 sites), and *Allium polyrhizum* (3 sites) fall in this category (see

Table 1) and were subjected to the analysis. This approach is acceptable because the variation of the parameters, Θ, ρ_0, and k determined above for each site was found small in the study areas.

The bidirectional reflectance data were then generated with BRDF for $\phi = 0^{\circ}$ and $\theta_v = 50^{\circ}$, whereas θ_s was selected from among 30°, 45°, and 60°, which cover the range of most θ_s values encountered in the field measurements. These were then converted into the tied spectra and used as inputs to the SUM approach to determine LCFs. The results were compared with visually determined LCFs, and the statistics of comparison are summarized in Table 2. Note that three LCF values are not independent and an increase of one LCF value will result in the decrease of others. Thus the comparison was made separately and independently for each LCF of PV, NPV and bare soil. An example of the comparisons is shown in Fig. 4 (a)-(c) for the case of *Stipa krylovii*. It can be seen that the agreement tends to get worse for larger θ_s, with larger RMSE values and smaller correlation coefficient. For PV and bare soil, the best agreement was for $\theta_s = 30°$, whereas for NPV, $\theta_s = 45°$ may be a better choice, although the difference is relatively small. In fact, a statistical test with *Z* score and *F* value (Motulsky & Ransnas, 1987) has indicated that the differences of *r* and RMSE for $\theta_s = 30°$ and $\theta_s = 45°$ were found not significant at both 0.01 and 0.05 levels. Thus, probably the effect of θ_s can be considered small for $30° \le \theta_s \le 45°$, and $\theta_s = 30°$ is a reasonable choice.

Next, the influence of θ_v for the LCF determination by means of SUM was investigated. In general, over the homogeneous surfaces, bidirectional reflectance increases with an increase of the off-nadir sensor view angle (Kimes, 1983). To test this effect, the same analysis applied above for θ_s was also carried out for θ_v; thus, θ_v was selected from among 30°, 50°, and 70°, whereas $\phi = 0^{\circ}$ and $\theta_s = 30^{\circ}$ were fixed in the application of SUM with BRDF. The resulting LCFs were compared with visually determined values in Fig. 5 (a)-(c) for the case of *Stipa krylovii*. The statistics of the comparison for all cases are listed in Table 3. The best agreement was found for θ_v = 50°, but the difference is small, except perhaps for the case of $\theta_v = 30^{\circ}$. A statistical test has shown that the differences of *r* and RMSE are not significant for θ_v = 30°, 50°, and 70° at both 0.01 and 0.05 levels. Thus, except perhaps for smaller θ_v values, LCF determination is not very sensitive to this angle selection. This can be explained by the fact that the effect of roughness becomes smaller, and the target can be treated as homogeneous for larger θ_v (Kimes, 1983). In the following analysis, the standard condition in the application of SUM was selected as $\phi = 0^{\circ}$, $\theta_s = 30^{\circ}$, and $\theta_v = 50^{\circ}$.

The reflectance obtained at different geometric view was converted to the above condition by means of BRDF before the SUM application. Fig. 6 shows the comparison of LCF values derived by means of SUM with spectra all converted for this standard condition by the BRDF function optimized for each site and those visually determined in the field for all 58 sites listed in Table 1. Also shown in Fig. 7 are the same comparison, but LCF estimates were obtained by SUM with the spectra data measured at $\phi = 0^{\circ}$ and $\theta_v = 50^{\circ}$ without application of BRDF angles conversion. In this case, θ_s is different among the points shown. The statistical analyses of the comparison are given in Table 4.

Several features can be noted. First, the difference in the agreement between the semi-arid and arid samples seems small, and thus, SUM is equally applicable to the surfaces in both regions in Mongolian steppe. Second, the LCF of the soil surface is not necessarily estimated more accurately than that of the others, although it is a simpler surface and of more uniform condition. This might have been caused by the disturbance of soil surface by the removal of the plant part as previously described. Even after such careful procedure, it is sometimes difficult to remove all smaller pieces of vegetation within the quadrat without causing damages to the soil surface. Third, the use of BRDF together with SUM tends to improve the accuracy of the LCF estimation. However, the difference is relatively small and is judged not significant by a statistical test with *Z* score and *F* value. This is not unexpected as the above results on the impact of measurement geometry have indicated that LCF estimations are not very sensitive to the geometry. Thus, measurements can be made over a less restricted condition than that adopted in the past. It is also interesting to note that the agreements obtained from the reflectance without the angle conversion by BRDF are approximately the same level as those obtained by Asner & Lobell (2000), whose results were obtained from the reflectance measured only within one hour of local noon on clear day. One clear advantage of the SUM application with spectral reflectance data without BRDF conversion is that it does not require spectral reflectance measurements from multiple angles of ϕ and θ_v. This is attractive because most reflectance data measured from an aircraft or possibly from a satellite are likely to be obtained for a single set of ϕ, θ_s, and θ_v. On the other hand, the determination of BRDF has an extra benefit of obtaining additional information about the surface. This can be used for various purposes such as for the validation and test of a radiative transfer model, estimation of radiation flux parameters, improved estimation of leaf area index, NDVI, and leaf inclination angles and distribution parameter, among others (e.g., Matsushima et al., 2005; Cui et al., 2009). Thus, it is still a good idea to adopt this strategy whenever it is feasible.

Finally, a comparison between the classified LCF values by means of SCM approach and those values visually determined is presented in Fig. 8, as a reference to the comparisons presented in Figs. 6-7. Clearly, SUM produces LCF estimates with better accuracy than the more traditional SCM approach with digital camera images. One also can note that among the results of SCM, LCF estimates for the bare soil show a larger scatter and contribute to the overall worse performance of SCM. The reason for this was further investigated by comparing the two examples of the SCM classification procedure (Fig. 9). When the classified images in panels (c) and (f) are compared with the original digital images in panels (a) and (d), it is clear that the bare soil and shadow cannot be distinguished from each other by the SCM; thus, together, they tend to occupy a larger percentage within the image. Attempts were made to classify the image into four elements—PV, NPV, bare soil, and shadows—without much success. One easy remedy would be to obtain images without any shadows; this may be accomplished by making measurements under complete cloudy skies without strong direct sunshine. However, it is possible that such images have weaker contrast among PC, NPV, and bare soil, and it is also not clear if this will not cause deterioration in the accuracy in LCF estimation. More studies will be needed in this aspect.

4. Conclusions

Hyperspectral data sets were obtained during intensive observations in the summer of 2005 and 2006 in semi-arid and arid steppe regions in Mongolia and were used in this study to test the applicability of the spectral unmixing model (SUM) to estimate land cover fractions (LCFs). The analysis has verified the results of earlier studies of Asner & Lobell (2000) and Asner & Heidebrecht (2002) for the American ecosystems that SUM is capable of producing LCFs in good accuracy, that the tied reflectance in the wavelength of 2000 – 2400 nm is most suitable for SUM, and that minimum of 50 combinations of wavelength selected at random by the Monte Carlo analysis are sufficient to produce LCF estimates. The accuracy of LCFs was highlighted by comparing the results from a more traditional method of supervised classification method (SCM) applied to the digital camera images. Thus, SUM with hyperspectral images seems to be applicable to a rather wide range of surface conditions that could be encountered in dry regions in American continents and also in Asian steppe regions. This is promising for remote sensing application from an aircraft or from a satellite.

In addition, the effect of measurement geometry represented by the solar zenith angle θ_s, the sensor view zenith angle θ_v, and the sensor azimuth angle ϕ to the LCF estimation was investigated. The bidirectional distribution function (BRDF) was first fitted to each data set to derive spectra at arbitrarily selected measurement geometry for use as inputs to SUM. Our results have shown that the LCF estimation is not very sensitive to these angles except perhaps for larger θ_s value and for smaller θ_v range. Among the acceptable range of angles, a better result was obtained for $\theta_s = 30°$, $\theta_v = 50°$, and $\phi = 0°$. Thus, measurements can be carried out over a larger portion of the daylight hours than those in the past. It also implies that the data obtained by remote sensing technology from various platforms at wide range of measurement geometry could also be useful to derive consistent LCFs by means of SUM approach.

As a final note, it should be pointed out that LCFs in the present analysis represent covers as viewed from above. Thus those hidden under the top-canopy are not accounted for. Although this is in accordance with general definition of the cover fractions, estimates of the layer-by-layer fractions may be necessary for a more complex canopy with multi-layer structure than the simple canopy present in the study areas. Clearly this is not possible with the approaches treated in the present study.

Acknowledgements

This study has been supported by the Japan Science and Technology Agency through grant under the Core Research for Evolutional Science and Technology (CREST) program funded for the RAISE (The Rangeland Atmosphere – Hydrosphere – Biosphere Interaction Study Experimental in Northeastern Asia) project. Partial support came from the Global Environment Research Fund of the Ministry of Environment of Japan and from University of Tsukuba Research Projects A.

References

Asner, G., & Lobell, B. (2000). A biogeophysical approach for automated SWIR unmixing of soil and vegetation. *Remote Sensing of Environment, 74,* 99-112.

Asner, G., & Heidebrecht, K. B. (2002). Spectral unmixing of vegetation, soil and dry carbon in arid regions: Comparing multi-spectral and hyperspectral observations. *International Journal of Remote Sensing*, *23*, 3,939-3,958.

Brutsaert, W. (1998). Land-surface water vapor and sensible heat flux: Spatial variability, homogeneity, and measurement scales, *Water Resource Research, 34,* 2433-2442.

Carlson, T., & Ripley, D. (1997). On the relationship between NDVI, fractional vegetation cover, and leaf area index. *Remote Sensing of Environment*, *62*, 241-252.

Chen, J., Jia, X., Yang, W., & Matsushita, B. (2009). Generalization of subpixel analysis for hyperspectral data with flexibility in spectral similarity measures. *IEEE Transactions on Geoscience and Remote Sensing, 47*, 2165-2171.

Cui, Y., Mitomi, Y., & Takamura, T. (2009). An empirical anisotropy correction model for estimating land surface albedo for radiation budget studies. *Remote Sensing of Environment*, *113*, 24-39.

Kimes, D. (1983). Dynamics of directional reflectance factor distributions for vegetation canopies. *Applied Optics, 22*, 1364-1372.

Li, S.-G., Asanuma, J., Eugster, W., Kotani, A., Liu, J.-J., Urano, T., Oikawa, T., Davaa, G., Oyunbaatar., & Sugita, M. (2005). Net ecosystem carbon dioxide exchange over grazed steppe in central Mongolia. *Global Change Biology, 11*, 1941-1955.

Li, X. B., Chen, Y. H., Yang, H., & Zhang, Y. X. (2005). Improvement, comparison, and application of field measurement methods for grassland vegetation fractional coverage. *Journal of Integrative Plant Biology*, *47*, 1074-1083.

Lobell, D. B., Asner, G. P., Law, B. E., & Treuhaft, R. N. (2002). View angle effects on canopy reflectance and spectral mixture analysis of coniferous forests using AVIRIS. *International Journal of Remote Sensing, 23,* 2247-2262.

Matsushima, D., Matsuura, Y., Byambakhuu, I., & Adyasuren, Ts. (2005). Estimating inter-and-Intra seasonal changes of satellite NDVI and LAI over Kherlen river basin using a bi-directional reflectance correction. *Proceedings of the First International Symposium on Terrestrial and Climate Change in Mongolia*, Ulaanbaatar, Mongolia, 137-140.

Motulsky, H. J. & Ransnas, L.A. (1987). Fitting curves to data using nonlinear regression: a practical and nonmathematical review. *FASEB Journal*, *1*, 365-374.

Painter, T. H., & Dozier, J. (2004). Measurements of the hemispherical-directional reflectance of snow at fine spectral and angular resolution. *Journal of Geophysical Research*, *109*, D18115, doi:10.1029/2003JD004458.

Privette, J. l., Eck, T. F., & Deering, W. D. (1997). Estimating spectral albedo and nadir reflectance through inversion of simple BRDF models with AVHRR/MODIS-like data, *Journal of Geophysical Research, 102*, 29529–29542.

Rahman, H., Verstraete, M., & Pinty, B. (1993a). Coupled surface-atmoshpere reflectance (CSAR) model 1. Model description and inversion on synthetic data, *Journal of Geophysical Research*, *98*, 20779-20789.

Rahman, H., Pinty, B., & Verstraete, M. (1993b). Coupled surface-atmosphere reflectance (CSAR) model 2. Semiempirical surface model usable with NOAA Advanced Very High Resolution Radiometer data, *Journal of Geophysical Research*, *98*, 20791–20801.

Roujean, L., Leroy, M., & Deschamps, P. (1992). A bidirectional reflectance model of the Earth surface for the correction of remote sensing data. *Journal of Geophysical Research*, *97*, 20455-20468.

Saandar, M., & Sugita, M. (2004). Digital atlas of Mongolian natural environments (1) vegetation, Soil, and Water. CD-ROM, Monmap Engineering Service Co., Ltd, Ulaanbaatar 210646, Mongolia.

Sasaki, M., Okayasu, T., Takeuchi, K., Undarmaa, J., & Jadambaa, S. (2005). Patterns of floristic composition under different grazing intensities in Bulgan, South Gobi, Mongolia. *Grassland Science, 51*, 235-242.

Shiirevdamba, Ts. (1998). *Biological Diversity in Mongolia, First National Report, Ministry for Nature and the Environment*. pp.106. Ulaanbaatar, Mongolia: Admon Printing House.

Sugita, M., Asanuma, J., Tsujimura, M., Mariko, S., Lu, M., Kimura, F., Azzaya, D., & Adyasuren, Ts. (2007). An overview of the Rangeland Atmosphere-hydrosphere-biosphere Interaction Study Experiment in Northeastern Asia (RAISE). *Journal of Hydrology, 333,* 3-20.

Susaki, J., Hara, K., Kajiwara, K., & Honda, Y. (2004). Robust estimation of BDRF model parameter. *Remote Sensing of Environment, 89*, 63-71.

White, M., Asner, G., Nemani, R., Privette, J., & Running, S. (2000). Measuring fractional cover and leaf area index in arid ecosystem: Digital camera, radiation transmittance, and laser altimetry methods. *Remote Sensing of Environment*, *74*, 45-57.

Willmott, J, C. (1982). Some comments on the evaluation of model performance. *Bulletin of the American Meteorological Society, 63*, 1309-1313.

Zhou, Q., Robson, M., & Pilesjo, P. (1998). On the ground estimation of vegetation cover in Australian rangelands. *International Journal of Remote Sensing*, *19*, 1815-1820.

Table 1 List of the observational sites with some observational results

Site name	Location		Time (LST)	Date	Sky condition	Land cover fractions (%)			Biomass (g / (0.25 m^2))		Soil moisture (%)	Vegetation species	Vegetation height (cm)
	Longitude (°)	Latitude (°)				PV	NPV	Bare soil	PV	NPV			
					Semi-arid								
KBU 1	108.74	47.22	10:40	31/07/2005	clear	35	55	10	16.9	33.5	9	*Artemisia adamsii*	11
KBU 2	108.74	47.21	11:25	31/07/2005	clear	45	50	5	18.4	52.8	10	*Stipa krylovii*	13
KBU 3	108.75	47.23	12:35	31/07/2005	clear	38	42	20	15.2	24.1	8	*Stipa krylovii*	14
KBU 4	108.74	47.22	15:40	31/07/2005	clear	30	15	55	12.2	20.6	12	*Carex duriuscula*	3
KBU 5	108.74	47.22	15:55	31/07/2005	clear	32	18	55	7.70	13.4	9	*Carex duriuscula*	4
KBU 6	108.74	47.22	16:35	31/07/2005	clear	25	15	60	13.9	27.3	10	*Potentilla tanacetifolia*	5
KBU 7	108.73	47.21	9:50	01/08/2005	clear	35	50	15	7.90	54.9	10	*Cleistogenes squarrosa*	3
KBU 8	108.73	47.21	11:10	01/08/2005	cloudy	40	10	50	7.30	3.50	9	*Cleistogenes squarrosa*	2
KBU 9	108.71	47.22	11:35	01/08/2005	cloudy	70	5	25	36.8	4.70	8	*Cleistogenes squarrosa*	10
KBU 10	108.71	47.22	12:11	01/08/2005	cloudy	75	5	20	14.3	7.30	8	*Chenopodium glaucum*	6
KBU 11	108.64	47.22	14:35	01/08/2005	cloudy	57	40	3	34.0	12.9	9	*Stipa krylovii*	15
JGH 1	109.31	47.31	10:10	02/08/2005	cloudy	45	25	30	9.10	24.2	14	*Potentilla tanacetifolia*	8
JGH 2	109.47	47.49	10:45	02/08/2005	clear	60	5	35	12.8	2.50	13	*Stipa krylovii*	3
JGH 3	109.50	47.50	12:20	02/08/2005	clear	60	5	35	11.2	0.90	36	*Artemisia adamisia*	5
JGH 4	109.48	47.51	15:25	02/08/2005	clear	55	10	35	10.9	10.7	13	*Stipa krylovii*	4
JGH 5	109.47	47.48	16:30	02/08/2005	cloudy	65	15	20	26.5	41.6	12	*Potentilla bifurca*	9
JGH 6	109.47	47.48	17:15	02/08/2005	cloudy	37	3	60	17.2	1.40	13	*Artemisia frigida*	5
JGH 7	109.47	47.48	17:55	02/08/2005	cloudy	55	5	40	27.8	8.90	15	*Kochia spp*	6
JGH 8	109.66	47.46	9:15	03/08/2005	cloudy	70	20	10	42.5	31.6	9	*Artemisia frigida*	13
JGH 9	109.74	47.40	10:05	03/08/2005	cloudy	80	10	10	42.2	22.3	10	*Artemisia adamsii*	15
UDH 1	110.02	47.38	11:55	03/08/2005	cloudy	65	10	25	24.6	11.2	10	*Stipa krylovii*	10
UDH 2	110.62	47.31	16:20	03/08/2005	clear	63	2	35	24.6	2.70	8	*Leymus chinensis*	8
UDH 3	110.62	47.31	17:15	03/08/2005	clear	85	5	5	80.6	76.6	8	*Stipa krylovii*	13
UDH 4	110.07	47.31	18:55	03/08/2005	clear	75	10	15	35.3	57.8	6	*Stipa krylovii*	20
UDH 5	110.67	47.26	9:25	04/08/2005	clear	80	10	10	38.0	17.2	8	*Stipa krylovii*	15
UDH 6	110.30	47.01	11:05	04/08/2005	clear	60	5	35	17.2	15.2	9	*Artemisia frigida*	13
DRN 1	109.66	46.80	13:05	04/08/2005	clear	65	5	30	21.7	4.00	6	*Leymus chinensis*	8
DRN 2	109.66	46.80	13:35	04/08/2005	clear	20	3	77	4.80	3.80	6	*Cleistogenes squarrosa*	5
DRN 3	109.41	46.63	13:36	04/08/2005	clear	25	10	65	8.20	2.20	6	*Leymus chinensis*	4
DRN 4	109.40	46.64	17:45	04/08/2005	clear	60	10	30	18.7	4.30	6	*Leymus chinensis*	3

DRN 5	109.40	46.64	19:05	04/08/2005	cloudy	75	5	20	8.40	2.80	8	*Leymus chinensis*	4
BGN 1	108.36	47.78	11:00	06/08/2005	cloudy	80	10	10	44.9	16.8	7	*Potentilla spp*	8
BGN 2	108.36	47.78	11:30	06/08/2005	cloudy	65	5	30	16.9	6.30	6	*Artemisia frigida*	5
BGN 3	108.36	47.78	12:00	06/08/2005	cloudy	80	5	15	51.1	2.20	7	*Artemisia frigida*	6
					Arid region								
MNG 1	106.41	45.86	8:50	02/08/2006	clear	30	5	65	11.5	0.80	7	*Allium polyrhizum*	12
MNG 2	106.41	45.85	9:40	02/08/2006	clear	40	1	59	12.4	0.70	6	*Allium mongolicum*	10
MNG 3	106.27	45.73	10:30	02/08/2006	clear	35	1	64	9.30	0.60	8	*Allium polyrhizum*	13
MNG 4	106.27	45.84	11:15	02/08/2006	clear	45	3	52	15.6	1.30	7	*Allium mongolicum*	14
MNG 5	106.27	45.83	12:05	02/08/2006	clear	80	5	15	16.8	1.80	6	*Convolvulus ammonii*	9
MNG 6	106.27	45.84	13:50	02/08/2006	clear	55	3	47	20.9	1.80	5	*Scorzyonera divaricata*	6
MNG 7	106.28	45.66	15:05	02/08/2006	clear	96	1	4	35.2	0.20	8	*Chenopodium album*	11
MNG 8	106.41	45.79	16:05	02/08/2006	clear	30	5	65	20.6	3.80	7	*Kalidium foliatum*	14
MNG 9	106.24	45.94	9:05	03/08/2006	clear	90	5	5	45.7	20.9	7	*Caragan microphylla*	20
MNG 10	106.24	45.92	9:50	03/08/2006	clear	70	5	25	10.5	2.70	6	*Chenopodium album*	7
MNG 11	106.25	45.92	10:15	03/08/2006	clear	65	5	30	13.1	1.60	7	*Artemisia acuminatum*	12
MNG 12	106.27	45.77	11:10	03/08/2006	clear	40	5	55	6.60	0.70	6	*Cleislogenes songorica*	7
MNG 13	106.47	45.81	13:25	03/08/2006	clear	40	5	55	12.7	0.50	6	*Arenaria capillaries*	7
MNG 14	106.47	45.81	14:30	03/08/2006	clear	15	5	80	8.50	0.30	9	*Bupleurum spp*	3
MNG 15	106.47	45.81	14:55	03/08/2006	clear	25	5	70	11.6	0.30	6	*Potentilla bifurca*	4
MNG 16	106.43	45.80	15:40	03/08/2006	clear	90	5	5	32.3	1.30	7	*Sibbaldiantha sericea*	3
MNG 17	106.43	45.80	16:55	03/08/2006	clear	35	5	60	16.6	1.20	8	*Allium polyrhizum*	10
BUL 1	103.66	45.01	8:45	05/08/2006	clear	35	5	60	9.50	0.20	6	*Peganum nigellastrum*	12
BUL 2	103.66	45.01	9:15	05/08/2006	cloudy	80	5	15	12.2	0.90	7	*Tribuls terrstric*	5
BUL 3	103.57	45.05	10:30	05/08/2006	cloudy	37	5	60	3.80	0.50	9	*Artemisia pectinata*	1
BUL 4	103.70	45.13	11:30	05/08/2006	cloudy	25	5	70	8.30	1.30	8	*Iris bungei*	12
BUL 5	103.64	45.25	14:15	05/08/2006	cloudy	10	5	85	4.10	4.50	4	*Stipa gobica*	2
BUL 6	103.64	45.25	14:40	05/08/2006	cloudy	10	5	85	4.80	0.60	6	*Oxytropis spp*	12
BUL 7	103.64	45.25	16:25	05/08/2006	cloudy	15	5	80	5.10	8.10	6	*Iris tenuifollia*	3

LST: local standard time, PV: photosynthetic vegetation, NPV: nonphotosynthetic vegetation, KBU: Kherlenbayan-Ulaan, JGH: Jargaltkhaan, UDH: Undurkhaan, DRN: Darkhan, BGN: Baganuur, MNG: Mandaligobi, and BUL: Bulgan. The biomass is given for dry weight.

Table 2 Statistics for the comparison between visually determined LCFs and estimated LCFs from SUM with BRDF for the three values of θ_s and from SUM without BRDF (raw spectra).

	Converted spectra by BRDF						Raw spectra	
Vegetation species	RMSE			r			RMSE	r
θ_s	30°	45°	60°	30°	45°	60°		
				Photosynthetic vegetation (PV)				
Stipa krylovii	4.09	4.60	6.38	0.97	0.93	0.98	4.28	0.95
Leymus chinesis	2.70	3.82	4.33	0.98	0.96	0.97	7.77	0.95
Cleistogenes squarrosa	3.04	4.52	4.59	0.98	0.96	0.98	5.00	0.98
Allium polyrhizum	5.11	6.09	7.67	0.74	0.74	-0.14	5.34	0.98
Combined	2.98	2.39	3.11	0.97	0.96	0.95	3.89	0.95
				Nonphotosynthetic vegetation (NPV)				
Stipa krylovii	2.89	2.74	5.06	0.98	0.97	0.94	4.99	0.95
Leymus chinesis	3.43	2.06	2.47	0.98	0.96	0.96	4.61	0.98
Cleistogenes squarrosa	1.70	3.31	1.68	0.98	0.96	0.98	4.86	0.85
Allium polyrhizum	3.56	2.38	6.03	0.91	0.25	0.28	4.08	0.76
Combined	1.23	1.39	3.27	0.98	0.98	0.96	2.88	0.96
				Bare soil				
Stipa krylovii	4.60	5.42	8.38	0.96	0.88	0.82	7.55	0.84
Leymus chinesis	1.86	2.42	5.92	0.83	0.96	0.96	5.62	0.94
Cleistogenes squarrosa	3.49	5.83	5.15	0.98	0.97	0.96	9.69	0.99
Allium polyrhizum	6.47	5.03	2.45	-0.38	0.84	0.97	7.84	0.98
Combined	2.37	2.68	4.66	0.96	0.96	0.95	4.33	0.95

RMSE: root mean square error, r: correlation coefficient. Sample number is 9 for *Stipa krylovii*, 5 for *Leymus chinesis*, 5 for *Cleistogenes squarrosa*, and 3 for *Allium polyrhizum*.

Table 3 Statistics for the comparison between estimated LCFs from SUM with BRDF for three values of θ_v and visually determined LCFs.

Vegetation species	RMSE			r		
θ_v	30°	50°	70°	30°	50°	70°
Photosynthetic vegetation (PV)						
Stipa krylovii	4.83	3.18	3.73	0.86	0.94	0.93
Leymus chinesis	6.24	4.60	4.36	0.95	0.98	0.99
Cleistogenes squarrosa	5.27	4.66	5.72	0.97	0.99	0.96
Allium polyrhizum	6.23	3.27	4.47	0.37	0.99	0.95
Combined	3.25	2.17	2.38	0.94	0.97	0.96
Nonphotosynthetic vegetation (NPV)						
Stipa krylovii	4.37	2.46	3.83	0.97	0.98	0.98
Leymus chinesis	2.49	3.38	2.90	0.76	0.80	0.96
Cleistogenes squarrosa	3.08	4.40	3.68	1.00	0.99	0.99
Allium polyrhizum	3.37	3.11	4.65	0.94	0.50	-0.14
Combined	2.23	1.81	2.35	0.98	0.99	0.98
Bare soil						
Stipa krylovii	2.64	4.39	5.18	0.92	0.97	0.87
Leymus chinesis	6.37	7.61	2.39	0.94	0.97	0.99
Cleistogenes squarrosa	6.38	4.18	5.14	0.98	0.98	0.93
Allium polyrhizum	6.49	5.49	7.09	0.13	0.99	0.40
Combined	2.20	2.09	2.80	0.95	0.97	0.96

Table 4 Statistics for the comparison between LCFs from SUM approach and those visually determined. For SUM, both raw reflectance data and converted data to the standard condition by means of BRDF were used.

Land cover type	RMSE		r	
	BRDF	Raw	BRDF	Raw
	Semi-arid area			
Photosynthetic vegetation	4.28	5.73	0.98	0.95
Nonphotosynthetic vegetation	3.49	3.33	0.98	0.98
Bare soil	5.72	5.74	0.97	0.96
	Arid area			
Photosynthetic vegetation	2.96	4.25	0.99	0.98
Nonphotosynthetic vegetation	2.09	2.12	0.52	0.25
Bare soil	3.43	4.35	0.99	0.98

Table 5 Statistics for the comparison between LCFs from SCM technique applied to HIS images and those visually determined.

Land cover type	RMSE	*r*
Semi-arid area		
Photosynthetic vegetation	9.02	0.87
Nonphotosynthetic vegetation	7.31	0.96
Bare soil	8.75	0.92
Arid area		
Photosynthetic vegetation	17.73	0.89
Nonphotosynthetic vegetation	6.43	0.42
Bare soil	19.25	0.85

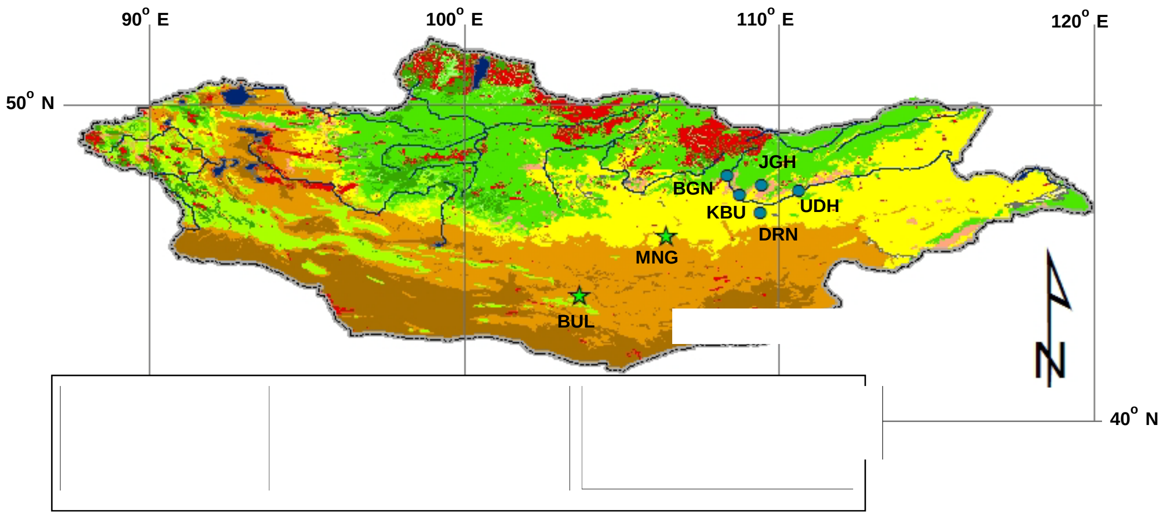

Fig. 1. Vegetation map of Mongolia (Saandar and Sugita, 2004) with the main observation sites of semi-arid and arid regions, major rivers and lakes. Circles represent observation points in semi-arid region, and stars represent those in arid area. Location names are as follows. JGN: Jargaltkhaan, BGN: Baganuur: KBU: Kherlenbayan-Ulaan: DRN: Darkhan, UDH: Undurkhaan, MNG: Mandalgobi, and BUL: Bulgan. The details of each site are listed in Table 1.

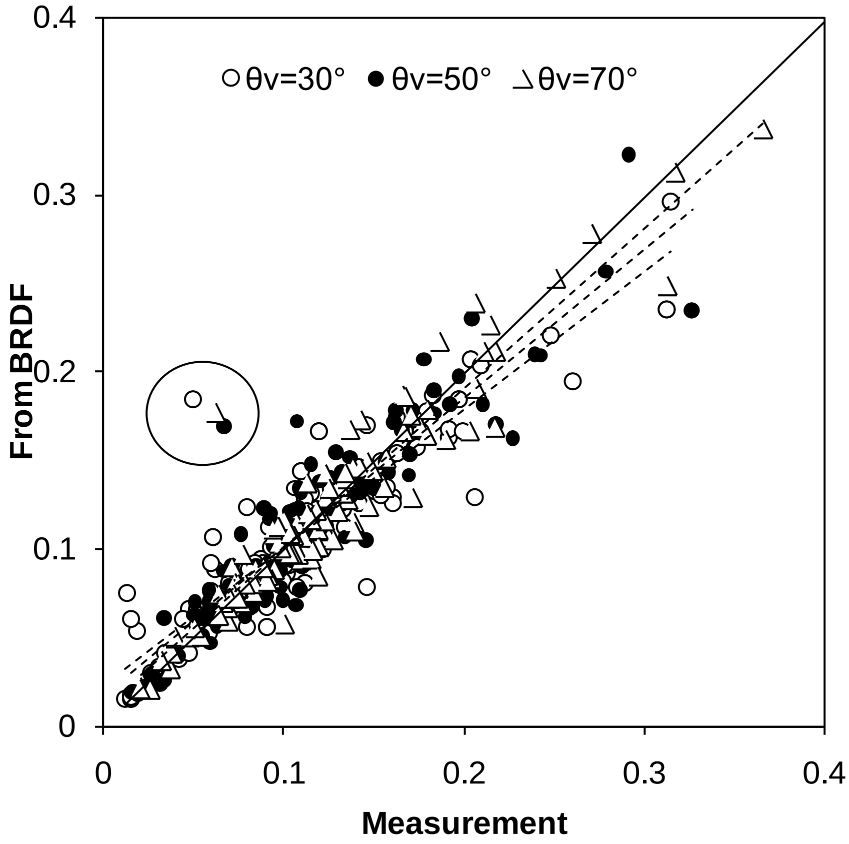

Fig. 2. Comparison between the reproduced reflectance by the BRDF function and measured reflectance values for the three off-nadir sensor view angles (θ_v = 30°, 50°, and 70°) and four azimuth angles (ϕ = 0°, 90°, 180°, and 270°). The circle indicates three outlier points from KBU11. The dashed lines indicate the regression equation $\hat{y} = a + bx$, (a = 0.022 and b = 0.73 for θ_v = 30°, a = 0.016 and b = 0.83 for θ_v = 50°, and a = 0.010 and b = 0.89 for θ_v = 70°), fitted to all points except for the outlier points.

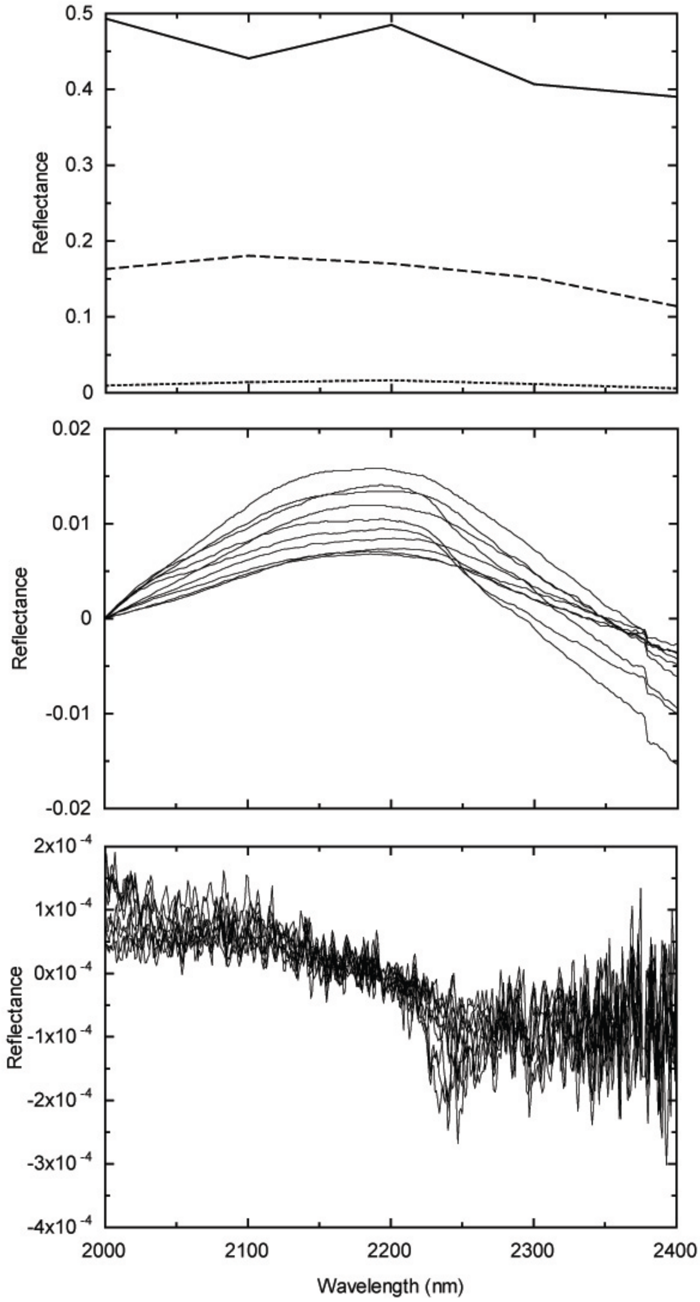

Fig. 3. Typical raw reflectance of PV (dotted), NPV (solid), and bare soil (dashed) (top panel); the tied reflectance of PV (middle panel); and the derivative reflectance of PV (bottom panel) in the range of 2000-2400 nm.

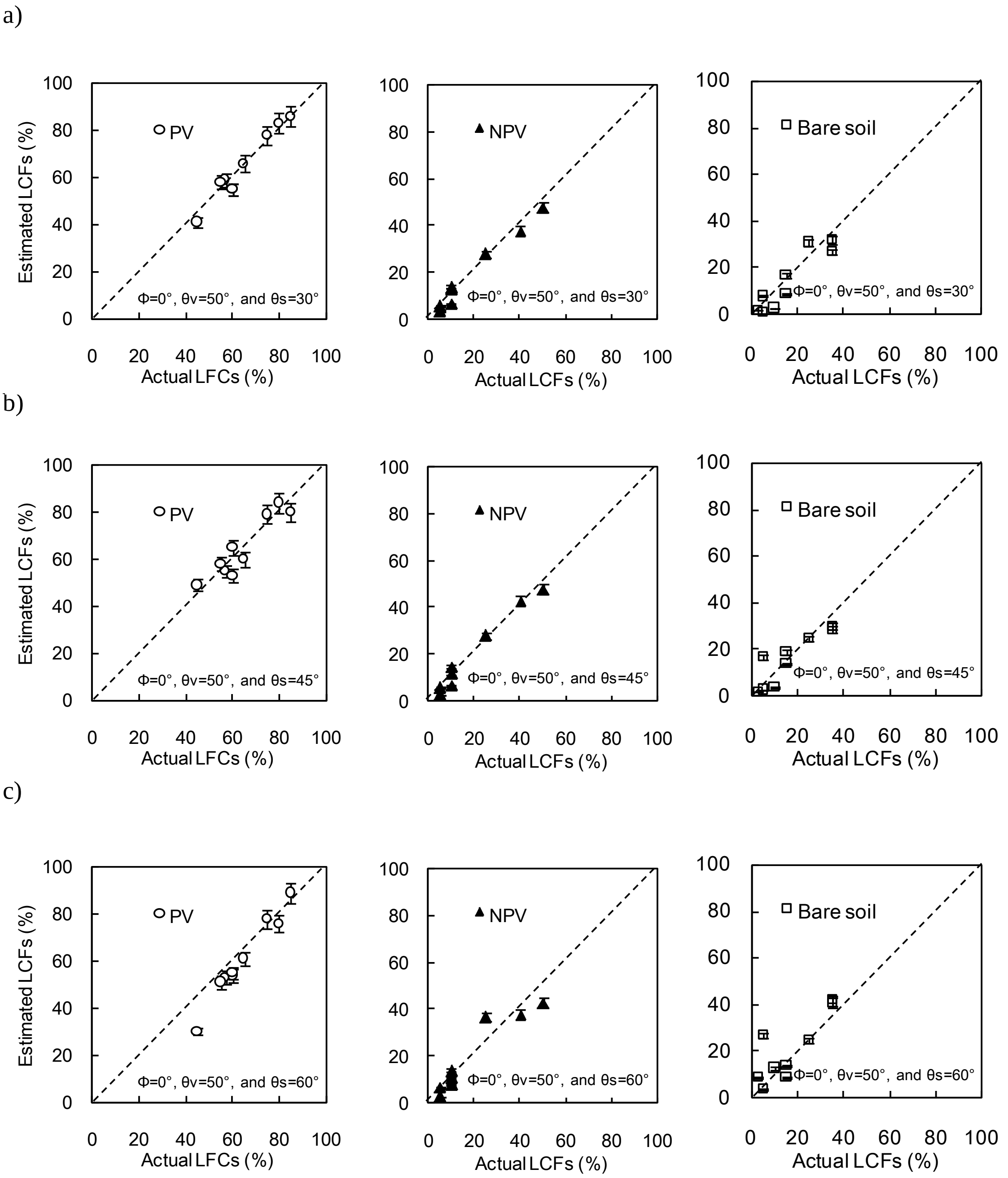

Fig. 4. Comparison of estimated and actual LCFs for *Stipa krylovii*. Panels a), b), and c) represent the results showing the effect of adopting different solar zenith angles θ_s =30°, θ_s =45° and θ_s =60°, respectively, whereas other angles are fixed at ϕ = 0° and θ_v = 50°. Symbols represent the mean, and the bars represent the standard deviation.

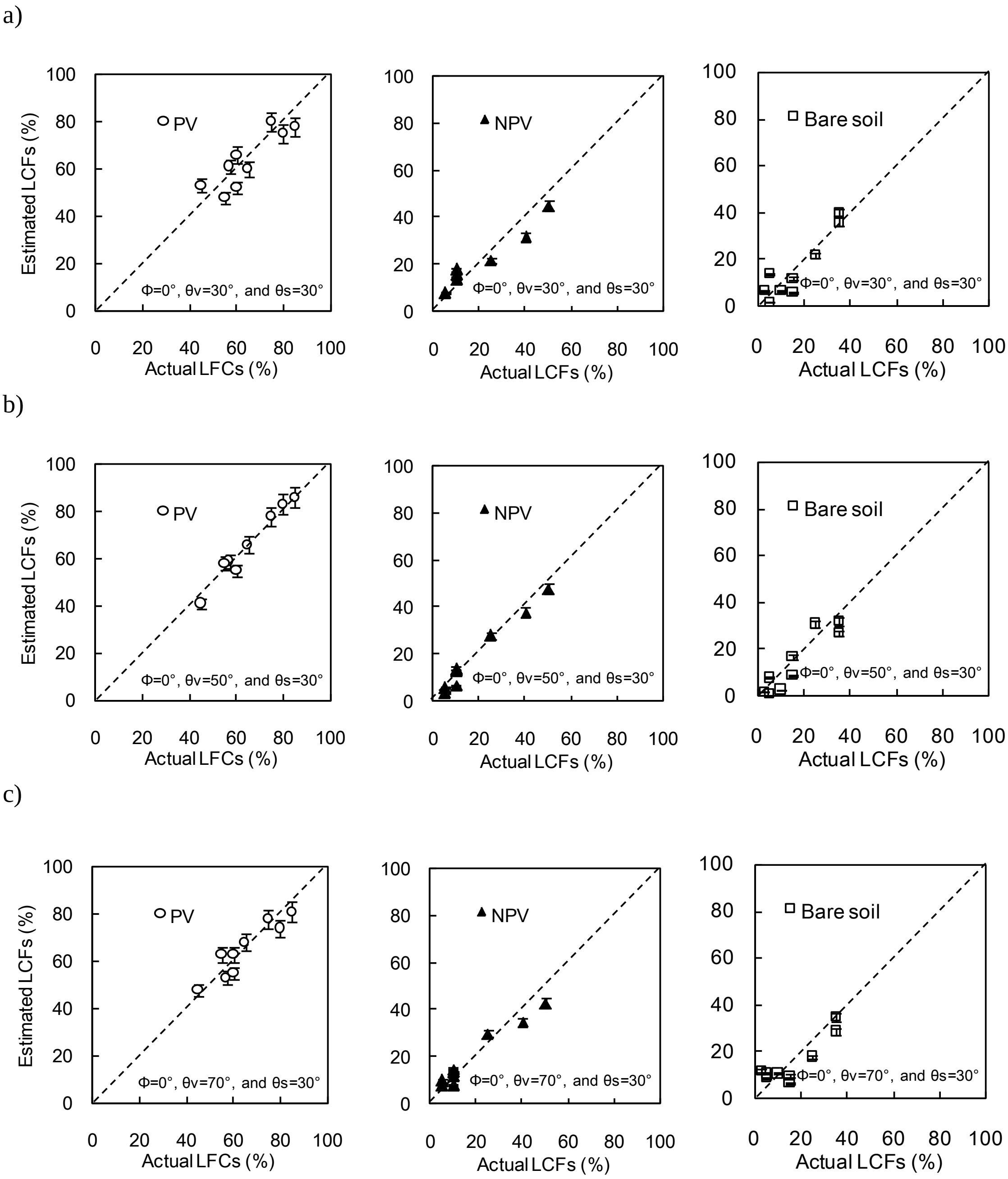

Fig. 5. Comparison of estimated and actual LCFs for *Stipa krylovii*. Panels a), b), and c) show the effect of using different sensor off-nadir viewing angles θ_v = 30°, θ_v = 50°, and θ_v = 70°, whereas ϕ = 0° and θ_s = 30° are fixed. Symbols represent the mean, and the bars represent the standard deviation.

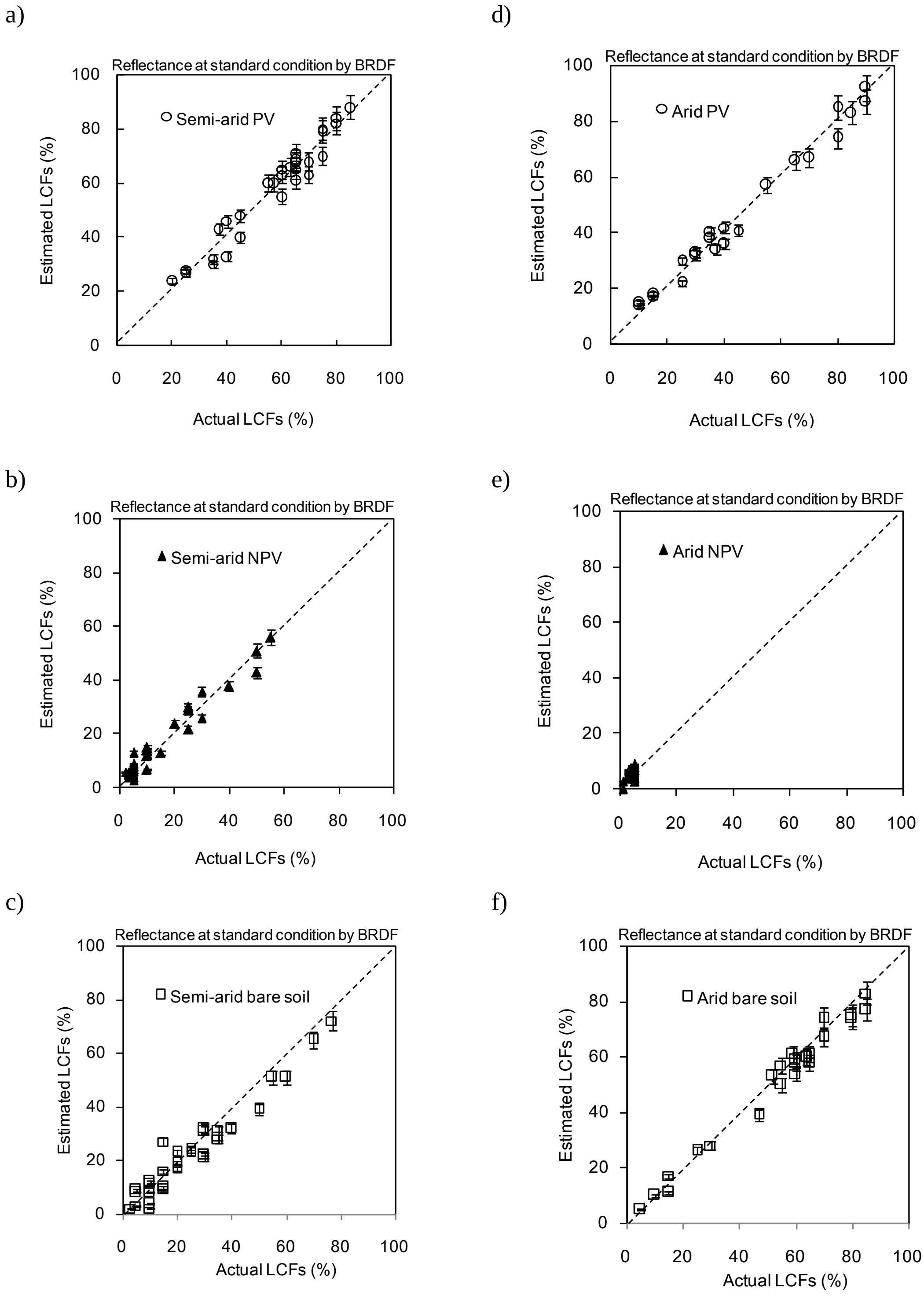

Fig. 6. Comparison of estimated and actual LCFs. The reflectance data set reproduced by BRDF for the standard condition of $\phi = 0^{\circ}$, $\theta_s = 30^{\circ}$, and $\theta_v = 50^{\circ}$. The left columns a), b), and c) represent the results for semi-arid area, and the right columns d), e), and f) represent those for arid area.

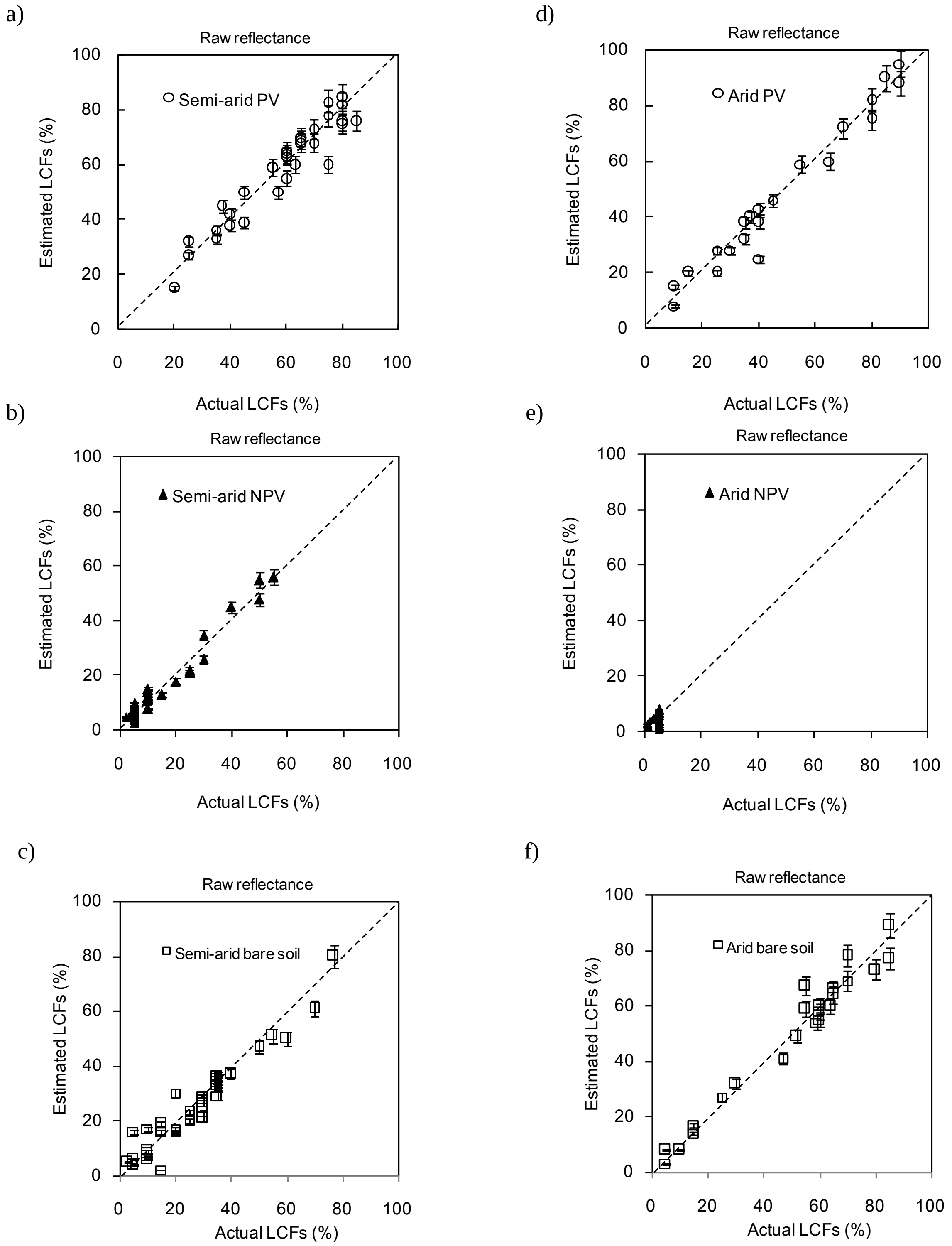

Fig. 7. Comparison of estimated and actual LCFs. The raw reflectance data set for $\phi = 0^\circ$, $\theta_v = 50^\circ$ and variable θ_s. The left columns a), b), and c) represent the results for semi-arid area, and the right columns d), e), and f) represent those for arid area.

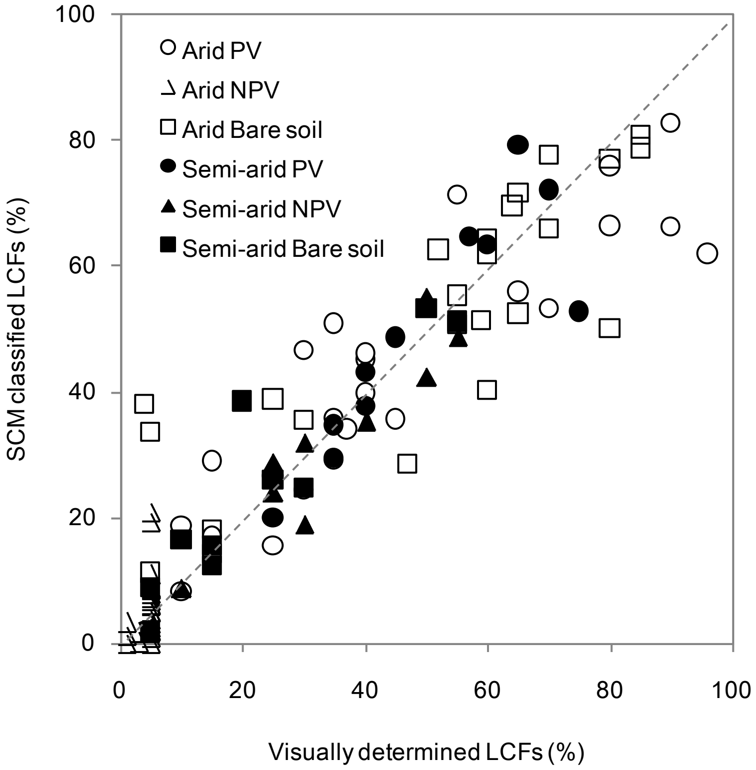

Fig. 8. Comparison of classified LCFs values and those determined visually. Both results for semi-arid and arid areas are shown. The solid line represents $y = x$.

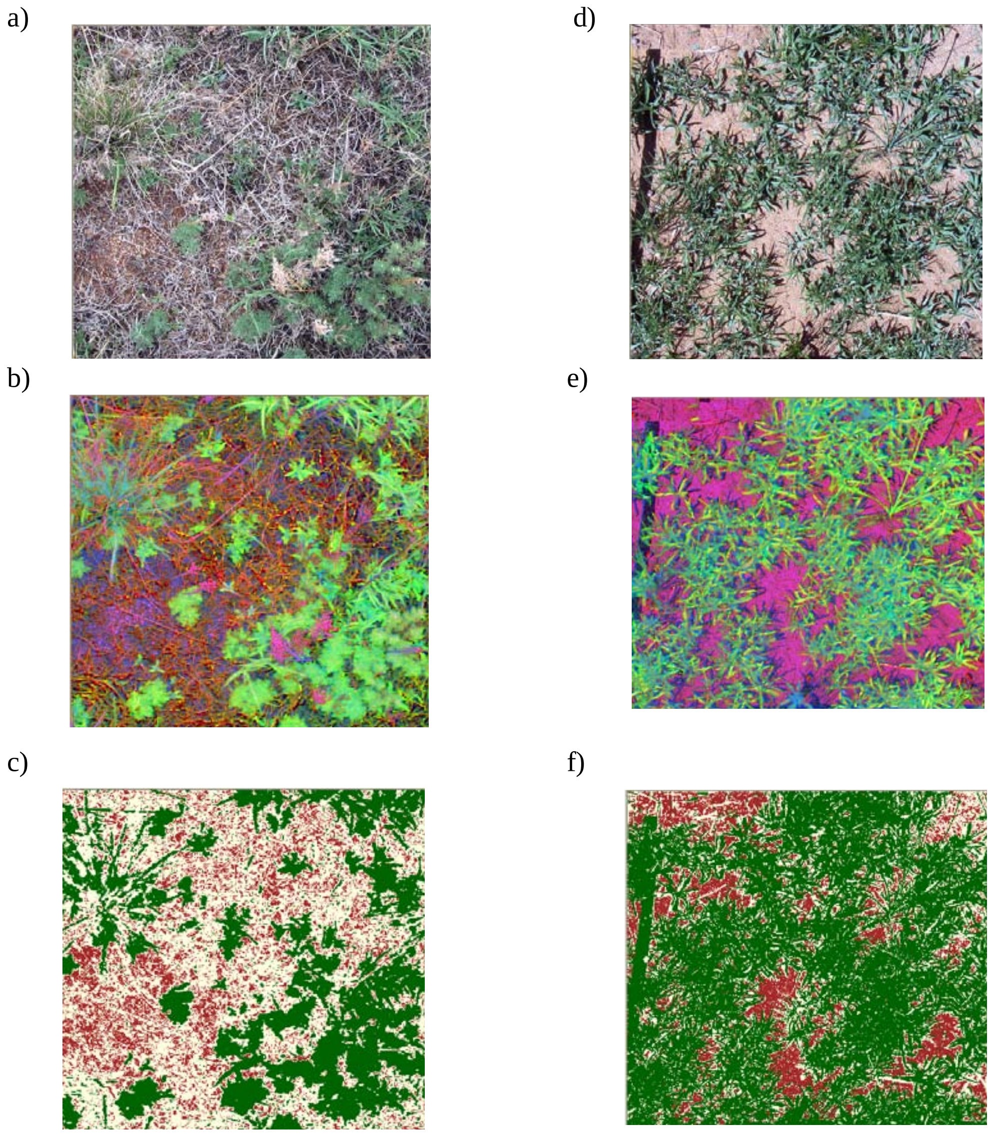

Fig. 9. Examples of LCF classification by means of SCM approach. The left columns a), b), and c) represent results for KBU1 site in semi-arid area, and the right columns d), e), and f) represent those for the MNG1 in arid region. The top side panels (a) and (d) show the original digital camera images, panels (b) and (e) are transformed IHS images, and panels (c) and (f) show the SCM classified images.